Sensing Water Properties at

Precise Depths from the Air

John-Paul Ore and Carrick Detweiler

Computer Science and Engineering

University of Nebraska-Lincoln, USA

`jore, carrick@cse.unl.edu`

Abstract

Water properties critical to our understanding and managing of freshwater systems that change rapidly with depth. This work presents an Unmanned Aerial Vehicle (UAV) based method of keeping a submerged, cable-suspended sensor payload at a precise depth, with 95% of sensor readings within ± 8.4 cm of the target depth. We use a depth altimeter attached at the terminus of a 3.5 m semi-rigid cable as the sole input to a depth controller actuated by the UAV's motors. First, we simulate the UAV-cable-payload system with disturbances of wind, water, signal delay, and GPS drift and then use parameters discovered during simulation to guide implementation. We characterize the depth altimeter during translation and find that 95% of readings are within ± 7 mm of ground truth, with a steady state error of ± 3 mm. In field experiments, we compare the depth precision of our new method to previous methods that used the UAV's altitude as a proxy for submerged sensor depth, specifically: 1) only using the UAV's air pressure altimeter; and, 2) fusing UAV-mounted ultrasonic sensors with the air pressure altimeter. Our new method reduces the standard deviation of depth readings from 16.1 cm to 4.2 cm in winds up to $8.0 \, \mathrm{m \, s^{-1}}$. We show the step response of the depth-altimeter method when transitioning between target depths. Finally, we explore a longer, 8.0 m cable and show that our depth controller still outperforms air altimeter and ultrasonic methods

Figure 1: UAV-system with a passive cable and sensors for measuring water properties at precise depths.

and allows scientists to increase the spatiotemporal resolution of water property datasets.

1   Introduction

Monitoring shallow surface water systems ($<10\,\mathrm{m}$) can be challenging for environmental and water scientists. Hindered by limited boat access, scientists are further constrained because boating and wading mix the water, disturbing the water properties under investigation. These water properties include temperature, conductivity, dissolved oxygen, and photosynthetically active radiation—all these vary significantly with small changes in water depth (Fischer et al., 2013; Chung et al., 2015; Higgins and Detweiler, 2016). These stratified properties are linked to ecosystem health and can predict imminent toxic algae blooms that threaten drinking water and fisheries and cost billions of dollars worldwide (Dodds et al., 2009; Anderson et al., 2010; Kudela et al., 2015; Sanseverino et al., 2016).

Currently, water scientists deploy static sensor arrays, often a collection of data-loggers vertically arranged underwater at a static position, and left for days or weeks. Some sensors used by water scientists require settling times (often $>3\,\mathrm{s}$), and existing water science datasets from static sensors have $\approx 0.25\,\mathrm{m}$ resolution in depth (Fischer et al., 2013). These static sensors yield datasets with good temporal resolution but are limited by poor spatial resolution because they have to be installed separately at each location. To increase the spatiotemporal resolution, our prior work presented the first

UAV-based water sampler (Ore et al., 2013), followed subsequently by several efforts (Schwarzbach et al., 2014; Ore et al., 2015; Rodrigues et al., 2015; Ribeiro et al., 2016; Koparan and Koc, 2016; DeMario et al., 2017; Akamatsu et al., 2017). In most of these efforts, the UAV flies above water while connected by cable to a sensor payload below water, as shown in Figure 1. Our follow-on work (Chung et al., 2015) explored a method of *in-situ* water temperature sensing at different depths with a UAV-based submerged sensor payload. However, the resolution of the resulting dataset was limited by poor control of the depth of the submerged sensor that wandered up and down as the UAV's air pressure altimeter drifted. The impact on the vertical resolution was compounded by sensor settling time (≈ 3 s).

To increase the depth resolution of water science datasets, this paper proposes and experimentally evaluates using a depth altimeter as input to a depth controller that seeks to minimize the target depth error using only the UAV's motors. These depth sensors are fast (50 Hz), light (<5 g), precise (± 3 mm), and affordable ($<\$30$ USD) and are already included in many underwater sensor payloads. Controlling depth using a submerged altimeter is challenging because the semi-rigid cable between the UAV and the submerged depth altimeter exhibits non-linear dynamics when bending and descending in water, especially in wind. We assume calm waters ('lentic', not flowing) and that the UAV is stationary. We first explore the feasibility of this approach in simulation including wind and water, then use parameters discovered in simulation to guide implementation, and finally test the implementation of our method in field experiments.

This work extends the conference version (Ore and Detweiler, 2018) by presenting a new system model, computational flow dynamics for wind drag, models of sensor noise and drift, detailed simulation results of wind gusts, sensor delay, sampling rate, and GPS drift, and also conducting new experiments to characterize the precision and accuracy of the depth altimeter.

Our contributions are:

- A new method of depth control to maintain a precise depth for a submerged sensor payload while passively connected by cable to a UAV. We use only a lightweight submerged depth altimeter, reducing the standard deviation of target depth errors from 16.1 cm to 4.2 cm compared with using ultrasonics rangefinders fused with pressure altimeter, the next best method. This method enables increased spatiotemporal resolution of

water science datasets without additional payload.

- Field tests of depth control, showing statistically significant reductions of depth variance in comparison to two previous methods: 1) air pressure altimeter alone; and, 2) air pressure fused with ultrasonic rangefinders. We compare these approaches using a 3.5 m cable for water depths down to 2.5 m.

- An initial exploration of using depth control with an 8.0 m cable, showing sufficient precision for sensing at greater depths.

This work presents an Unmanned Aerial Vehicle (UAV) based method of keeping a submerged, cable-suspended sensor payload at a precise depth, with 95% of sensor readings within ± 8.4 cm of the target depth ($\sigma = 4.2$ cm), using only a lightweight submerged depth altimeter. The paper is organized as follows: Section 2 shows connections between this work and previous environmental monitoring with autonomous systems and also describes some related water science techniques; Section 2 describes our approach to the problem and includes simulation results for common environmental disturbances like wind and GPS drift; Section 4 examines our system architecture and shows results from characterizing the depth altimeter; Section 5 details the results of three field experiments, including a comparison of depth precision between flight modes and an initial exploration of an 8.0 m cable; Section 6 discusses how the simulations compare to results in the field and identifies lessons learned; Section 7 indicates possible future directions of this research; and Section 8 summarizes the work.

2 Related Work

Previous efforts relate to our current work in several ways: either water scientists measure surface water properties, or a UAV is used to measure water properties, or autonomous surface / underwater vehicles (ASVs and AUVs) are used to measure water properties, or a UAV makes a pose and altitude estimation in unknown environments, or a UAV has a cable-suspended load.

Water scientists often measure water properties by leaving data-loggers at field locations for days or weeks a time (Dodds, 2002; Fischer et al., 2013). Often these sensors are arranged vertically in the water column at fixed intervals along a rope (Chung et al., 2015), with the rope pulled down by an anchor and pulled up by a buoy. These

sensors are used to measure water phenomenon that varies sensitively by depth (MacIntyre et al., 2002), such as temperature, conductivity, dissolved oxygen, and photosynthetically active radiation. In keeping with existing water science method, and for compatibility with existing datasets, our method takes measurements vertically at a single location and does not attempt to translate laterally with our submerged sensor payload. Our previous work (Chung et al., 2015) shows that moving the sensor payload up and down in the water column does not cause significant mixing that could bias the measurements.

Several efforts seek to use UAVs to monitor water properties using cable-based sensor payloads (Schwarzbach et al., 2014; Ore et al., 2015; Koparan and Koc, 2016; DeMario et al., 2017; Akamatsu et al., 2017; Song et al., 2017). These systems use air pressure altimeters to estimate altitude, and like these efforts, we seek to sense subsurface water properties with a cable-connected payload, but unlike these works, we focus on precise depth control. Systems like the fixed-wing Flying Fish (Eubank et al., 2009) maintain persistent observation of surface properties, but cannot detect subsurface properties. Some efforts propose amphibious UAVs (Rodrigues et al., 2015; Bershadsky et al., 2016; Ribeiro et al., 2016), and like this work we are interested in the advantages offered by UAVs to water monitoring, but unlike this work we seek to minimize water column mixing, that can take hours to settle. Our previous work presents evidence that sensing by a small, submerged sensor payload (≈ 2 *cm* diameter sensor, 0.7 *cm* cable) does not cause a mixing disturbance that impacts water temperature measurements (Chung et al., 2015).

In environmental monitoring, (Dunbabin, 2016) uses multiple ASVs to sample greenhouse gasses, while underwater the MARES AUV system samples water quality for a long duration at depths up to 100 *m* (Cruz and Matos, 2008). Garneau *et al.* (Garneau et al., 2013) used an ASV to monitor cyanobacteria. (Zhang et al., 2015) explore water columns with a gliding, fish-like robot, and the WaterBug (Higgins and Detweiler, 2016) descends passively in a water column to collect a single water sample at a target depth. Unlike these systems, we want to quickly deploy and redeploy to disconnected or difficult to reach water bodies.

Several efforts (Hollinger and Sukhatme, 2014; Yoo et al., 2015; Das et al., 2015; Ma et al., 2017; Lawrance et al., 2017; Alam et al., 2018) use an information quality metric (e.g. information gain or variance reduction) along with system constraints (e.g. battery) to plan motion during environmental monitoring in aqueous environments, mostly with AUVs and ASVs. These works plan a path and choose a waypoint (or depth) based on a data-driven metric,

whereas our work assumes the target depth has already been chosen. Our proposed method is compatible with and could benefit from selecting target depths based on adaptive sampling.

Several approaches seek to estimate altitude for micro UAVs in unstructured outdoor environments, including *et al.* (Jain et al., 2015), who autonomously explored rivers and estimated altitude using specular laser returns to estimate the plane of the river surface. Unlike this work, we seek a method that minimizes the payload devoted to non-water-property sensing. (Burri et al., 2015) use a stereo camera and IMU to map and estimate a pose in a previously unknown environment, but these methods have not been demonstrated over water, to our knowledge. Our previous work (Ore et al., 2015) explores the use of fusing downward-facing ultrasonic sensors with an air pressure altimeter, and we use this method for comparison in the current work.

Several efforts model and control cable-suspended payloads from a UAV (Tang and Kumar, 2015; Goodarzi et al., 2014), but assume that the cable can be observed. We likewise use a cable-suspended payload but do not attempt to observe or model the cable's dynamics during flight.

3 Technical Approach

This section describes our approach to the problem of obtaining precise depth control of a submerged sensor payload. We seek to retain the benefits of monitoring water properties by UAV while adding minimal system complexity. Overall, our approach is to simulate the dynamics, sensing, and control of the system to establish feasibility and determine baseline system performance requirements, like signal delay and sampling rate. The simulations include control and dynamics of the UAV, wind gusts, GPS drift, sensor delay, depth altimeter sampling rate, depth altimeter sensor noise, and water drag on the submerged sensor payload. In the rest of this section, we discuss each of these simulation elements in detail, show the outcomes of the simulations, and discuss key simulation results.

3.1 Simulation Elements

Our system model is shown in Figure 2 and consists of: A) UAV; B) dangling cable; and, C) sensor payload. The forces acting on the system include the total thrust from the UAV F_{thrust}, wind F_{wind}, drag on the submerged sensor
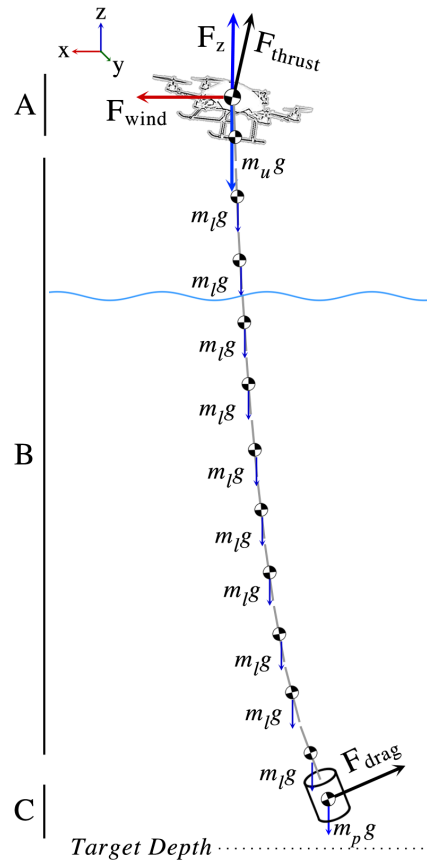
Figure 2: Model of UAV-system used in simulation, showing the suspended cable as a series of rigid links.

F_{drag}, and gravity. The figure also shows the portion of UAV thrust that directly opposes gravity, F_z, that is actuated by the depth controller. Table 1 shows a list of simulation parameters and the values used.

UAV Dynamics and Control. The stability and accuracy of the system depend on the interplay between the UAV-cable-payload system and the environment. Therefore the UAV's dynamics and control are important to model. The UAV model is based on an AscTec Firefly hexacopter (Achtelik et al., 2012), with a total mass of $m_u = 1.0$ kg including battery, and a maximum thrust of 36 N. The UAV's thrust is the only actuator, and the UAV is modeled as a 6-DOF spherical mass. We implemented a cascaded position-derivative (PD) attitude and position controller, similar to (Meyer et al., 2012), with velocity and thrust parameters from the UAV's datasheet (Ascending Technologies, 2012). We tuned to P and D terms by hand to match the performance of the real system. We use a PD controller for lateral position because we observed in the field that an integral term struggles in wind turbulence and a precise position in x and y (<3 m) is not required in this application as long as the location is known. Changes to the UAV's roll and pitch in response to external disturbances (like wind) can cause small errors in depth because the cable is attached 4 cm below the center of mass, but the depth controller treats this error like any other disturbance and adjusts F_z accordingly. Figure 3 shows the design of the depth controller that attempts to minimize the error between target depth and readings from the submerged depth altimeter. As shown in the figure, the depth altimeter readings are run through a Kalman Filter without the control input, because the transfer function involves the non-linear dynamics of the cable that we do not model.
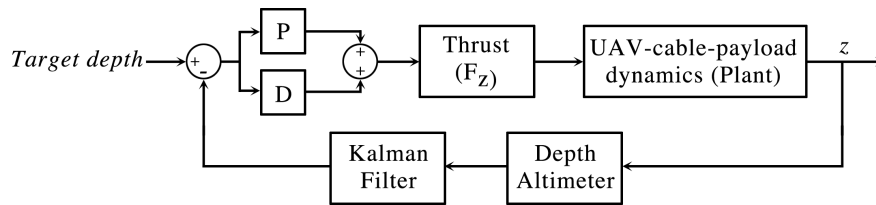

Figure 3: Depth control using the UAV's thrust, specifically only the portion of thrust that opposes gravity, F_z. The UAV-cable-payload dynamics are the plant.

We do not model the UAV's state estimator that might include input from accelerometers and gyroscopes, because small changes (<3 m) in the UAV's position in x and y are not critical to the scientific value of sensor readings, unlike the small changes in z that are only controlled with respect to the depth sensor. Therefore the impact of omitting the error in UAV pose estimation to our model is likely small and simplifies the model.

We want to calculate the force, F_{wind}, exerted on the UAV given a lateral wind velocity, v_w. We start by considering the drag equation:

$$F_{wind} = \frac{1}{2} \rho_a A_u C_u v_w^2 \tag{1}$$

Where ρ_a is air density at $15\,°C$, A_u is the UAV's cross-sectional area, and C_u is the drag coefficient. We first combine all the constants into the value k_u:

$$k_u = \frac{1}{2} \rho_a A_u C_u \tag{2}$$

Then substitute k_u into Equation 1:

$$F_{wind} = k_u v_w^2 \tag{3}$$
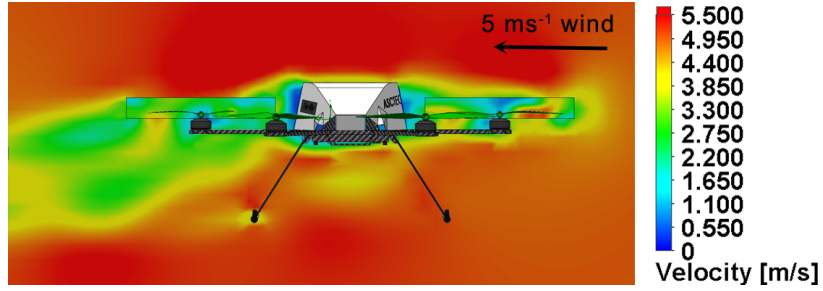
Figure 4: Simulated airflow velocity on a hovering AscTec Firefly used to estimate air drag force, F_{wind}. The figure shows a constant lateral $5\,\mathrm{m\,s^{-1}}$ wind.

To estimate k_u for our UAV, we use Solidwork's computation fluid dynamics (CFD) to calculate the drag force, F_{wind}, over a range of wind velocities from $1.0\,\mathrm{m\,s^{-1}}$ to $10.0\,\mathrm{m\,s^{-1}}$ and simulate with the average force estimate, $F_{wind} = 0.258\,\mathrm{N}$ at $v_w = 5.0\,\mathrm{m\,s^{-1}}$. Figure 4 shows the resulting CFD simulation showing the downwash from the UAV's spinning propellers during hover in wind. Using these values in Equation 3, we solve for k_u and find $k_u = 0.010\,\mathrm{kg\,m^{-1}}$. Table 1 shows a summary of all the parameters used during simulation. Knowing k_u allows us to solve for the wind force, F_{wind}, given a wind velocity, v_w. We use Equation 3 during the UAV-cable-payload simulations to apply a force to the UAV over a range of wind velocities.

Submerged Sensor Payload. The sensor payload includes the depth altimeter modeled as a cylindrical mass of $m^p = 18\,\mathrm{g}$ attached at the cable terminus. The resistance from water shown in Figure 2, F_{drag}, limits the payload's velocity. We want to calculate the force, F_{drag}, as a function of the payload's velocity in water, v_p.

We again start with the drag equation, but this time for the payload's drag in water:

$$F_{drag} = \frac{1}{2}\rho_w A_p C_p v_p^2 \tag{4}$$

Where ρ_w is water density at $15\,°C$, A_p is cross-sectional area of the sensor payload, and C_p is the drag coefficient. We first combine all the constants into the value k_p:

$$k_p = \frac{1}{2}\rho_w A_p C_p \tag{5}$$

Then substitute into Equation 4:

$$F_{drag} = k_p v_p^2 \tag{6}$$

Now we solve for k_p, substituting the gravitational force on the payload's, $m_p g$ for F_{drag}:

$$k_p = \frac{m_p g}{v_p^2} \tag{7}$$

We know $m_p = 18\,g$ and conduct an experiment to measure the payload's terminal velocity, v_t, in water. We release the payload at the top of a translucent 3 m water test tank (≈ 0.25 m radius by 3 m) tall and measure the time at which the payload reaches markings of depth 1 m and 2 m. Using six observations, we estimate the average terminal velocity, v_t, to be $-0.54\,\mathrm{m\,s^{-1}}$. By setting $v_p = v_t$ in Equation 7 we obtain $k_p = 0.605\,\mathrm{kg\,m^{-1}}$.

With an empirical value for k_p in Equation 4, we can solve for the payloads drag force in water, F_{drag}. We use F_{drag} from Equation 6 to model how the payload will move in water. The force F_{drag} reduces the payload's descent rate to slower than the UAV's descent rate, creating a hazard of the UAV outpacing the depth sensor and flying toward the water. Therefore we limit changes to the target depth to 1 m and eventually will implement velocity control as part of the depth controller. Decreasing the target depth by increments of $<$1 m allows the payload to descend fast enough to match the descent of the UAV.

Cable. The dangling cable is modeled as a series of 16 rigid links suspended directly underneath the UAV's center of mass *et al.* (Goodarzi et al., 2014) and connected by a series of 2 DOF joints, as shown in Figure 2. We use a total cable length of 4 m based on conversations with our water science collaborators, who indicate that 3 m depth is sufficient to characterize many shallow lakes and stream confluences (Chung et al., 2016). We divided the 4 m cable into 16 lengths following the approach in (Goodarzi et al., 2014). We tried using 30 links and obtained similar depth

error results but in substantially more simulation time. We weighed a cable, also from our current work to calculate that each 0.25 m link has a mass of $m_l = 3.8$ g. We assume the water drag on the cable is small compared to the drag on the sensor payload because the cable mostly moves up and down during translations between depths and it has small surface area profile when suspended vertically in the water. Every link joint has a small damping constant to reduce oscillations in the cable. The swinging, dampening, and overall behavior of the simulated cable appears consistent with observations of real UAV cable systems.

3.2 Simulation Disturbances

Now that we have a model of the UAV-cable-payload system, we consider common environmental and system disturbances. Based on our experience, we assume that the biggest disturbances would be: 1) wind gusts; 2) GPS drift; and, 3) signal delay and sampling rate of the depth readings. We now consider each of these disturbances and describe the results in Section 3.3.

Wind Gusts. Wind gusts are important because as the UAV is blown laterally, the submerged payload will be pulled away from the target depth, and gusts might make the depth controller unstable. We consider wind gusts at intervals of $1 \, \mathrm{m \, s^{-1}}$ up to $10 \, \mathrm{m \, s^{-1}}$, the limit specified for the Firefly UAV by the manufacturer.

We model wind gusts as an instantaneous force, F_{wind}, acting on the system starting from an ideal case, where the UAV-cable-payload system is vertical with zero velocity. For a given wind velocity, v_w, F_{wind} is determined by Equation 1 and assumes that the air drag constant k_u does not change with UAV's attitude since the UAV is assumed to be near hovering. We add noise to wind gusts using Von Kármán Wind Turbulence (Kármán, 1937) used by the U.S. Military (United States Department of Defense, 1997). The turbulence magnitude scales with wind velocity, but in winds of $10 \, \mathrm{m \, s^{-1}}$, it is bounded by $\pm 10 \, \mathrm{m \, s^{-1}}$.

GPS Drift. GPS drift is important because we suspect that lateral translations, without depth control, directly impact depth accuracy. We simulate GPS drift using a Gauss Markov error model (Brown and Hwang, 1997; Meyer et al., 2012). Gauss Markov is useful for modeling GPS drift because the bias 'wanders' over time. Specifically, a GPS

position reading $y(t)$ at time t is:

$$y = \hat{y} + b + w_a \tag{8}$$

$$\dot{b} = \frac{1}{\tau}b + w_b \tag{9}$$

Where $\hat{y}$ is the original reading, b is the bias, and w_a is white Gaussian noise. The change in bias over time is $\dot{b}$, where τ is a time constant and w_b is white Gaussian noise. We set $\tau = 0.25$ to make the change in bias consistent with readings from the real system. The noise and bias and updated at 5.0 Hz, based on the uBlox GPS receiver unit on the AscTec Firefly.

Signal Delay and Sampling Rate of the Depth Altimeter. We model signal delay because of the multiple network hops for depth readings: from depth altimeter to embedded system to control computer and back to the UAV as shown in Figure 11. Signal delay and sampling rate are important to model because they indicate performance requirements for implementation. We model an offboard control computer because this what we use during field experiments. Implementing an onboard controller is more complex for prototyping, but would likely reduce signal delay. We assume that the impact on the simulation will be at least as much as the impact on the real system. We expect that the impact of signal delay and sampling rate will be most acute during vertical translations between target depths. Therefore, we simulate a range of delays and rates without other disturbances to isolate the impact of these factors. We include simulation of extreme values, like a 1500 ms delay and a very slow sampling rate of 0.5 Hz even though these values are unrealistically pessimistic, to show nearly unstable system responses.

Air Pressure Altimeter Control. For comparison, we model air pressure altimeter control because it is one of the previous modes that is used commonly in other efforts. This is not a system disturbance like wind gusts, but instead a different method of maintaining a target depth. This uses the UAV's built-in air pressure altimeter to maintain a specified air altitude as a proxy for target depth. We model the drift and error in the air pressure altimeter using the Gauss Markov error model shown in Equation 8-9. In our previous work (Ore et al., 2015), we characterized air pressure altimeter drift during steady-state tests, and in these simulations chose parameters that matched field observations. In the field, we observed small oscillations over $3-5$ s seconds and larger drift over 30 s. We set the time constant $\tau = 30$ in Equation 9, meaning that the value drifts towards a new value over the course of 30 s.
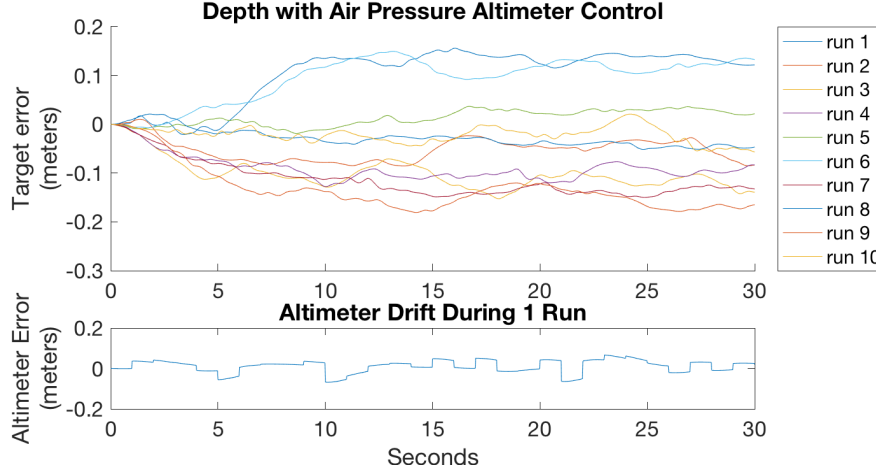
Figure 5: Depth error with air pressure altimeter control, our previous method used in standard UAV controllers. Errors of this magnitude (σ =11.05 cm) reduce the spatial resolution of water science datasets.

3.3 Simulation Results

All simulations begin from the ideal state, vertical with zero velocity, and are subject to disturbances for 30 s. In the ideal case, when the UAV moves up, the sensor payload is directly coupled, and when the UAV moves down, the only forces acting on the payload are gravity and resistance from water, F_{drag}. Below we present simulation results for GPS drift, wind gusts, sensor delay and sampling rate. All of the simulations use the depth controller, except the air pressure altimeter simulation that uses the UAV's altimeter as a proxy for depth.

Air Pressure Altimeter Results. For comparison, we simulated the standard control method of using the UAV's air pressure altimeter as a proxy for submerged depth. Figure 5 shows the result of 10 simulations with air pressure altimeter control. In these simulations, the standard deviation of depth readings ($\sigma = 11.05$) means 95% of simulated depth readings are within ±22.1 cm of the target depth. As expected, air pressure altimeter control yields insufficient depth resolution, motivating our depth control approach. This simulation shows that the pressure altimeter control is not accurate enough, and therefore we need to rely on a better sensor like the depth altimeter. The subsequent simulations presented below use our new depth control method that is not influenced by transient air pressure fluctuations.

Signal Delay and Sampling Rate Results. These simulations test -1.0 m step responses over a range of signal delays and sampling rates from the depth altimeter. Figure 6 shows the depth readings of the UAV-cable-payload system over
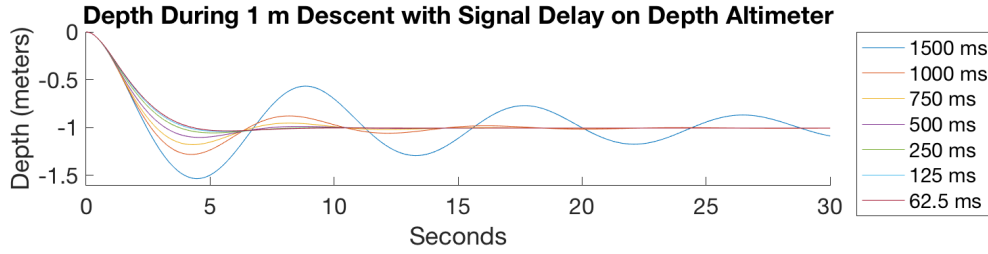
Figure 6: Impact of signal delay on target depth during 1.0 m translation, sampling rate held constant at 10 Hz. Signal delay >125 ms causes overshoot while translating between depths.

a range of signal delays with the sampling rate held at 10 Hz. As shown in the figure, shorter delays result in faster convergences with less oscillation. To avoid overshooting the target depth, a delay of <125 ms is required. When reducing the delay from 125 ms to 62.5 ms, there is only a modest improvement therefore we set a goal for signal delay of <100 ms.
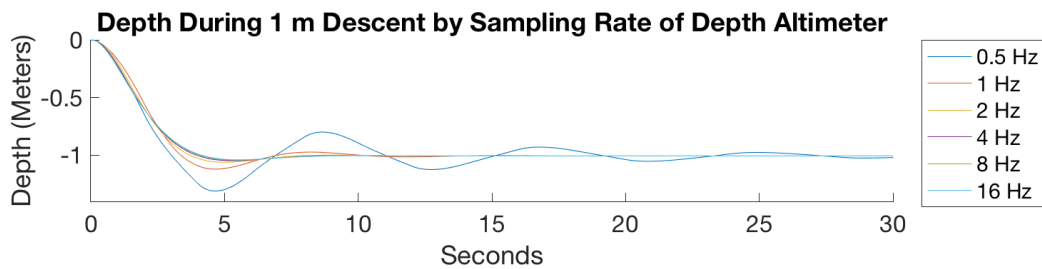
Figure 7: Impact of sampling rate on target depth during 1.0 m translation, single delay held constant at 100 ms. Sample rates <8 Hz causes overshoot while translating between depths.

Figure 7 shows the system response over a range of depth sensor sampling rates with the signal delay held to 100 ms. As shown in the figure, to avoid overshooting caused by sampling rate, >8 Hz is required, but 16 Hz reduces the time to converge by only a small amount. Although the overall stability depends on a combination of parameters, the signal delay and sampling rate parameters individually can cause the simulated system to become less stable. These simulations suggest bounds for delay and sampling rate. During simulation, the system could still converge quickly to the target depth with a slow sampling rate of 2 Hz, and with little improvement from 8 Hz to 16 Hz. Therefore we consider 10 Hz to be a sufficient sampling rate.

GPS Drift Results. Figure 8 shows the target error in 10 simulations, subject to the GPS sensor noise from Equa-

tions 8-9. As shown in the figure, the depth target error is bounded by ± 5.0 cm, with a standard deviation $\sigma = 1.6$ cm. The bottom part of the figure shows a sample of simulated GPS drift error in x for one run, consistent with GPS readings from the field.
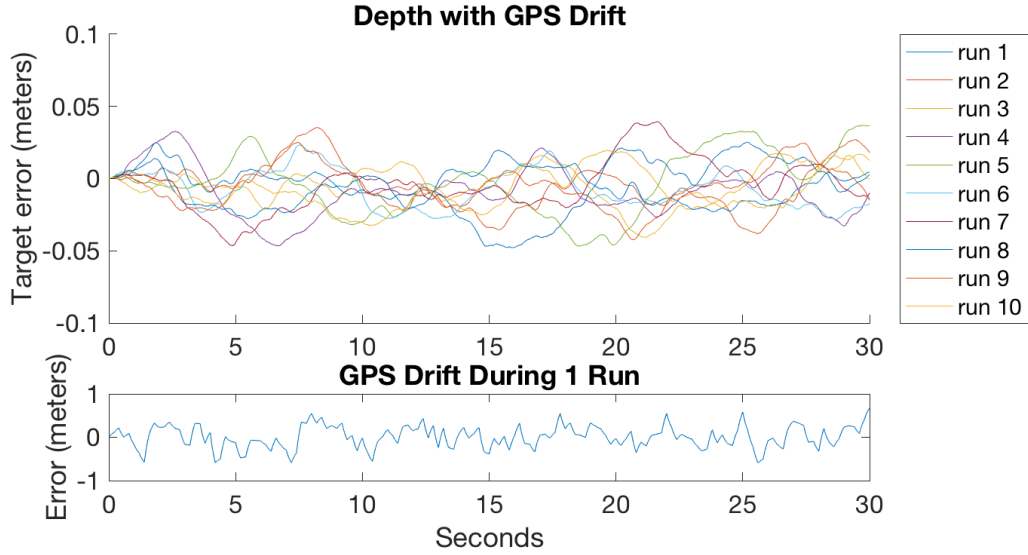

Figure 8: Depth altimeter readings in 10 simulations response to wind gusts with GPS drift. The bottom part of figure shows GPS drift error in x during a simulation run.

Wind Gust Results. Figure 9 shows the result of 10 simulations over a range of wind gust velocities, from $10\,\mathrm{m\,s}^{-1}$ down to $1\,\mathrm{m\,s}^{-1}$ at $1\,\mathrm{m\,s}^{-1}$ increments. As shown in the figure, the target depth error grows with the magnitude of the wind gust. For all wind gusts, during the first ≈ 2 s, the target depth error is increasingly positive as the sensor payload is pulled up in the water as the UAV is blown laterally off course, also indicated in Figure 2. After the sensor payload is pulled up above the target depth, it then 'plunges' in the water as the UAV descends and simultaneously the cable is pulled straight by gravity. Note that the response shown in Figure 9 might appear to be overshooting from an excessive P term, but really the plunge in target error is a consequence of the interplay between the cable, water, depth controller, and gravity. As shown in the figure, the target error moves back towards zero with some depth error caused by turbulence in the wind model.

The bottom part of Figure 9 shows the UAV's altitude during a $10\,\mathrm{m\,s}^{-1}$ gust, showing how it descends as it pitches against the gust, reducing the portion of the thrust vector directed against gravity. Although a $10\,\mathrm{m\,s}^{-1}$ wind might blow a micro-UAV off course by $1-3$ m meters, the simulations suggest that this will only cause a depth target error

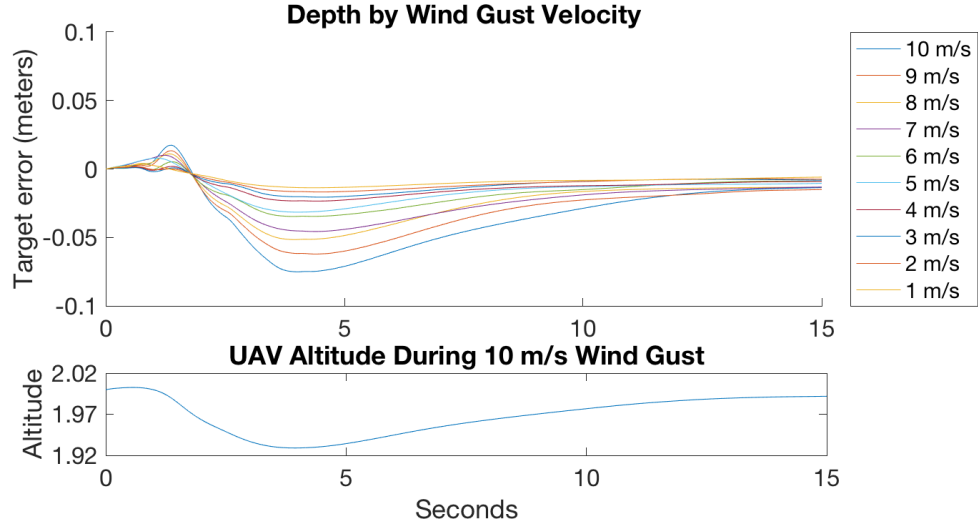**Figure 9:** Simulated depth altimeter readings in response to wind gusts up to $10\,\text{m s}^{-1}$ at $1\,\text{m s}^{-1}$ intervals. Bottom part of figure shows UAV's altitude during $10\,\text{m s}^{-1}$ wind gust.

of $\pm 10\,\text{cm}$. We expect the real system will be operated in winds less than $10\,\text{m s}^{-1}$. For wind gusts, the depth standard deviation is $\sigma = 2.8\,\text{cm}$.
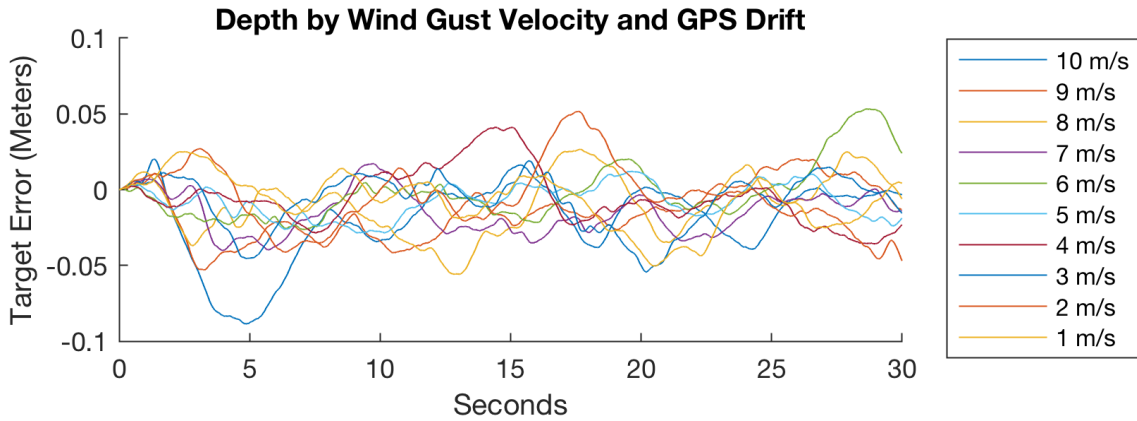

Figure 10: Simulated depth altimeter readings for 10 runs in response to simultaneous wind gusts, GPS drift, sensor delay and sampling rate disturbances.

All Disturbances Combined Results. In the field, we expect all these disturbances simultaneously: signal delay, wind gusts, sampling rate, and GPS drift. Therefore we simulated the system's behavior with all disturbances over a range of wind gusts, and the results are shown in Figure 10. The signal delay and sampling rate used in these simulations was 100 ms and 10 Hz respectively—values based on the simulation results. As shown in the figure, the depth target

error is bounded by ± 10 cm. All disturbances combined is not significantly worse than GPS drift alone, as can be seen by comparing Figures 10 and 8. For wind gusts with GPS drift, 95% of depth readings are within ± 5.2 cm of the desired target.

Key Simulation Results Overall, simulations indicate that the system can achieve the desired target depth resolution, even in response to wind gusts of $10 \, \mathrm{m \, s^{-1}}$, near the manufacturer's limit. Here are the key takeaways we learned from simulation:

- Depth altimeter sampling frequency should be ≥ 10 Hz.
- Signal delay from the depth altimeter to UAV control input should be ≤ 100 ms.
- Small transient lateral disturbances from wind or GPS drift do not cause the system to become unstable, and also do not compromise depth accuracy.
- Air pressure altimeter control is insufficient for the desired depth resolution.
- Depth control with the depth altimeter is sufficient for the desired depth resolution.

We now use these simulation results to guide our implementation.

4   Implementation Details

This section explains the system architecture, characterizes the depth altimeter, and describes the three flight modes used during experiments.

4.1   System Architecture

Figure 11 shows the system architecture used during experiments, consisting of 1) shoreside control computer and RC controller; 2) UAV with an embedded system; and, 3) submerged system with sensor payload.

The Firefly includes a GPS and air pressure altimeter as well as an onboard controller for attitude and position. We chose the Firefly for overwater experiments because it can return to shore even after one motor fails. It has a payload
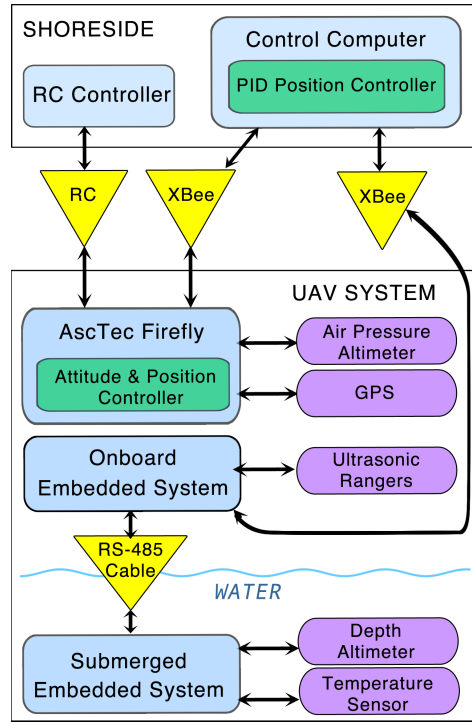
Figure 11: System Architecture.

capacity of 600 g, flies for 15-20 minutes per battery, and tolerates winds up to $10\,\mathrm{m\,s^{-1}}$.

The sensor payload installed on the Firefly consists of two embedded systems, the first installed on the vehicle and the second waterproof system attached to the end of the cable that dangles below the UAV. The first embedded system has an NXP-LPC2368 (ARM7TDMI) microprocessor running a control loop at 50 Hz, and has inputs for a variety of water sensors and is used to log and transmit real-time readings over the radio. The submerged embedded system contains an ATmega-1284pb microprocessor that reads the depth altimeter at 50 Hz. The embedded system installed on the UAV receives the depth readings and re-transmits them to the control computer. The control computer is an Apple MacBook "Early 2015" running Ubuntu 14.04 with ROS Jade for control and logging.

In this architecture, we estimate the complete signal delay from the depth altimeter to the UAV control input to be 45 ms worst case, based on measurements and an analysis of the communication systems. This is within the 100 ms bound identified during simulation and described in Section 3.3.

4.2 Depth Altimeter Characterization

For the depth altimeter, we use a Measurement Specialties MS5803-01BA (Measurement Specialties, 2015) installed on an embedded system, and shown in Figure 12. By the datasheet, this sensor is water resistant to 100 m with a built-in 24-bit ADC and a 10 ms read time, plus an additional 10 ms to read the onboard thermometer to correct for temperature variation. By reading from the onboard thermometer, the depth altimeter can operate over a range of temperatures, from $-40\,°C$ to $85\,°C$ as specified on the datasheet. The 10 ms total means a maximum sampling frequency of 50 Hz and this is what we use, above the baseline 10 Hz indicated by simulation.

To better understand the performance of the depth altimeter we seek to characterize its steady-state error, lag time, accuracy, and precision. Although the datasheet specifies the altimeter's steady-state error, lag time, accuracy, and precision, our implementation and waterproofing might influence this crucial sensor. Understanding the behavior of the depth altimeter is critical because it is used for both depth control and comparison with to other methods during field experiments. To characterize steady-state error, we placed it at a fixed depth in a bucket of $22\,°C$ water. Figure 13 depicts 10 s of readings and shows a steady-state error of ± 3 mm.

To characterize the depth altimeter's response time and accuracy, we compared the depth readings to ground truth readings captured by a Vicon motion capture system. The experimental setup is shown in Figure 14. As shown in the figure, we built a 2.0 m water tube and an upside-down 'U-shaped' rigid linkage between the depth altimeter and Vicon markers. When we move the linkage assembly up and down, both the depth altimeter and the Vicon markers
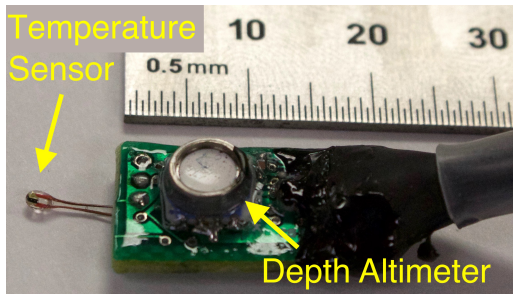

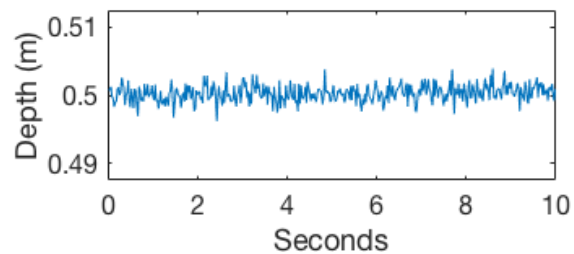**Figure 12:** The waterproof embedded system and sensor payload.

Figure 13: Depth altimeter steady-state error at constant depth showing ± 3 mm error. This measured error is used the system simulations discussed in Section 3.1.
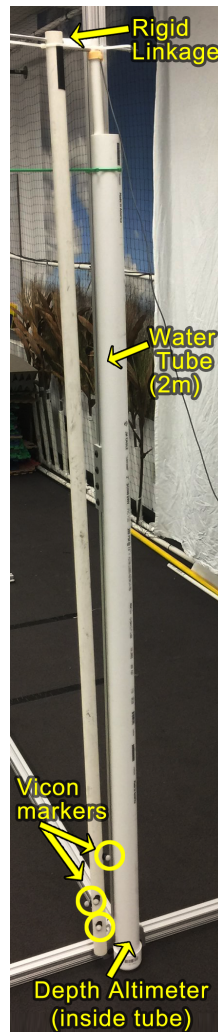
Figure 14: Water-tube apparatus (2.0 m) to characterize depth altimeter error.

move together. Figure 15 shows the results, and how closely the depth altimeter tracks Vicon position data. Figure 16 zooms in on 10 s. Notice that during the 20 cm decent between 40 and 42 s that there is negligible lag, and sometimes the depth altimeter leads Vicon, possibly due to variable Vicon latency.

Figure 17 shows a distribution of depth altimeter sensor errors with respect to Vicon from the step response shown in Figure 15. As shown in the figure, 95% of depth altimeter readings are within ± 7 mm of Vicon ($\sigma = 3.5$ mm). We characterized the sensor down to 2.0 m depth, and the manufacturer's datasheet indicates $<0.5\%$ error down to 12 m. Because of the MS5803's fast response, accuracy to depths of 10 m, and small steady-state error, we use this sensor for comparison during our field experiments.

It is important to note that changes to ambient air pressure cause pressure changes in water, impacting depth readings. For example, an air pressure difference of 100 mbar across a strong weather front results in 0.6 m pressure difference measured in water depth. In practice, the depth altimeter must be calibrated for the current air pressure every few hours by submerging the sensor to a known depth (we used 5 cm). However, during a 20-minute flight, the total air pressure change is likely small, and transient air pressure fluctuations like wind that cause an air altimeter change of ± 2.0 m cause a depth altimeter change of only ± 3 mm. This makes sense since water is ≈ 800 times denser than air.

4.3 Flight Modes: Depth, Air Pressure, Ultrasonic + Air Pressure

We implement three flight modes: depth altimeter, air pressure altimeter, and ultrasonic altimeter. The depth altimeter mode is the new method proposed and implemented in this work, and the air pressure and ultrasonic modes are alternative methods for comparison during experiments. Note that the depth altimeter method controls depth while air pressure and ultrasonic methods control the UAV's altitude as a proxy for sensor depth.

Depth altimeter mode controls only depth using the portion of the UAV's thrust that opposed gravity, F_z, as shown in Figure 2, while the UAV controls roll, pitch, and yaw. On the control computer, the stream of depth readings is passed through a Kalman filter assuming Gaussian noise (characterized in Section 4.2), and we assume a linear state transition function during hover. The filtered readings are used in a 50 Hz PD position controller (described in Section 3.1) for depth that commands the thrust opposing gravity, F_z.

Air pressure altimeter mode uses the UAV's onboard controller for everything: roll, pitch, thrust, and yaw. Air pressure mode uses the UAV's air pressure altimeter, GPS, and an onboard IMU together to create a fused pose estimate. This is the basic 'out-of-the-box' controller.

Ultrasonic altimeter mode fuses downward-facing ultrasonic sensors with the air pressure altimeter to form an altitude estimate. We include ultrasonic mode because: 1) we used it in our previous work (Chung et al., 2015); 2) ultrasonics rangefinders are accurate to within ± 1.0 cm over water at close range (<1.85 m) (Ore et al., 2015) and can be used in combination with spooling mechanism; 3) to obtain variable depth readings; and, 4) this mode is roughly similar in altitude accuracy to Lidar using specular returns (Nuske et al., 2015). To prevent the ultrasonic sensors from seeing the cable, the readings from each of the two ultrasonic sensors (Maxbotix MB1240-EZ4 (Maxbotix, 2018)) are pre-filtered based on both the variance of recent readings and the proximity of readings to the current altitude estimate, before being passed through a Kalman filter. The details of this pre-filtering are described in previous work (Ore et al., 2015).

Now that we have an implementation guided by simulation, we discuss experimental validation in the field.

5   Field Experiments

This section describes the setup of field experiments and presents results. To test our approach, we designed three field experiments:

1. A comparison of depth precision for three flight modes with a 3.5 m cable and submerged sensor payload;

2. Step responses to changes in target depth for the proposed depth altimeter method;

3. Initial exploration of the depth altimeter method using a longer, 8.0 m cable, measuring precision and step response.

All field experiments were conducted during March, 2017 at Wildwood Lake near Lincoln, Nebraska, USA, as shown in Figure 18. Wildwood has relatively still water, and is similar to the kinds of shallow surface water system we target in this work. In total, we flew 33 missions. The comparison dataset was collected during three days, and the

wind average speeds were $3.5\,\mathrm{m\,s^{-1}}$, $2.0\,\mathrm{m\,s^{-1}}$, and $1.3\,\mathrm{m\,s^{-1}}$, respectively with a maximum 5-second wind speed of $8.5\,\mathrm{m\,s^{-1}}$, $7.2\,\mathrm{m\,s^{-1}}$, and $7.9\,\mathrm{m\,s^{-1}}$, respectively, indicating occasional strong gusts. We measured wind speed and direction using a weather station recording into a time-synced computer log.

5.1   Experiment 1: Comparison of Flight Modes for Maintaining Constant Depth.

The purpose of this experiment is to compare three flight modes and quantify how precisely we can maintain the depth of a sensor payload. We collect depth readings in each of the three modes while maintaining a specified depth, and then measure the difference in variance between the modes. The three modes are detailed in Section 4.3.

We launched the vehicle from a jetty to a sampling location $10\,\mathrm{m}$ from shore, indicated in Figure 18. For these experiments, we used a $3.5\,\mathrm{m}$ cable affixed below the UAV's center of mass (see Figure 2). For each mission, we flew to the sampling location by a human pilot, descended until the depth altimeter was at least 1 m deep, then switched to one of the computer controlled flight modes. Once in computer control mode, the system attempts to remain stationary in x and y while recording depth. We flew two modes per flight, each for $\approx$240 s. It can be difficult to compare the results of different outdoor trials, so within a single flight we tested different flight modes successively, and recalibrated the depth altimeter every few hours to adjust for changing air pressure. We swapped the flight mode sequence between trials to ensure that no mode benefited from fresher batteries. In total, we flew 36 minutes, 12 minutes in each mode maintaining a specified depth. We use the depth altimeter reading for comparison, as it is accurate and fast as described in Section 4.2, and use this as a basis for evaluating the target depth precision.

Figure 19 shows the distribution of depth readings collected during the three flight modes. The data are collated from 3-4 flights per mode. To compare the variances of depth readings collected in each mode, we use a F-test (Box, 1953), and find significant differences between the variance of depth control mode and ultrasonic mode ($p < 0.0001$), and between depth control mode and ultrasonic mode ($p < 0.0001$). Since F-tests can be sensitive to non-normal distributions and our distributions are only approximately normal ((Shapiro and Wilk, 1965) test for non-normality indicates a non-normal distribution with $p < 0.0001$), we also compared the variance using a Fligner-Killeen (Fligner and Killeen, 1976) test and confirmed the significant differences in variance ($p < 0.0001$).

As shown in Figure 19, the depth altimeter mode is significantly more precise than either ultrasonic or air pressure modes. Specifically, the statistical dispersion of depth readings in depth altimeter mode keeps 95% of readings within ± 8.4 cm ($\sigma = 4.2$ cm) from the target depth. This is within our goal of being able to obtain readings with a resolution of at least ≈ 25 cm. The depth readings for the ultrasonic altimeter are slightly offset and centered near -0.03 m due to calibration. The ultrasonic-pressure altimeter mode shows $\sigma = 16.1$ cm, or 95% of readings within ± 32.2 cm, while the air altimeter has the largest dispersion, with 95% of readings within ± 60.2 cm ($\sigma = 30.1$ cm) of the target depth.

To give the reader better intuition about the variation of depth readings in each mode, Figure 20 shows examples of 4 minutes of continuous flight for each mode along with the 5-second-average wind speeds. As shown in Figure 20(a), depth altimeter mode stays closest to the target depth with almost no drift and small disturbances, and note that it maintained this target depth during 5.0 m s^{-1} wind gusts. Also, note in Figure 20(b) how ultrasonic altimeter mode is not as precise and occasionally deviates almost a meter even with calmer winds, but does not drift significantly over time, unlike the air pressure altimeter mode. The variations are likely caused by transient atmospheric pressure differences and noise. During the ultrasonic altimeter test, we moved the UAV closer to the water so that the ultrasonic rangefinders could get better readings, resulting in greater depth compared to the other two methods. In Figure 20(c), the air altimeter mode depth readings change by $30-40$ cm in a small amount of time, but that within two minutes the depth readings can be off by ± 0.75 m. The large drift in air pressure mode is likely caused by significant changes in ambient air pressure, like the wind.

5.2 Experiment 2: Step Response of Depth Altimeter Mode for a 3.5 m Cable

To determine if the system under depth altimeter control could transition between target depth reference points, we conduct 'step response' maneuvers. Figure 21 shows the step responses under depth altimeter control. For each reference depth, we set the system to hold a particular target depth, then adjust the target by 0.5 m. Notice how the reference depths are repeatable both ascending and descending and the depth quickly settles to within ± 5 cm of the target depth. For comparison, Figure 22 shows the step response for air pressure altimeter mode. We do not show the step response for ultrasonic altimeter mode because it only works well when close to the water. We use 0.5 m changes to avoid the UAV outpacing the submerged sensor toward the target depth, until we implement a descent velocity limit,

reserved for future work.

5.3 Experiment 3: Longer 8.0 m Cable: Target Error and Step Response

As an additional experiment, we extended the cable length to 8.0 m. The reason we are interested in a longer cable is that in some applications we want to be able to measure water properties across a range of depths, nearly all <10 m, and we also wanted to see what impact a longer cable would have on the ability to control the depth. Therefore, we field tested the depth altimeter flight mode with the 8.0 m cable. The experimental setup is identical to the depth altimeter mode tests in Sections 5.1-5.2 other than the longer cable length. We were only able to test the 8.0 m cable down to a depth of ≈ 4 *m*, due to depth limitations at our field location.

Figure 23 shows the results for holding a target depth, and for comparison, the figure shows the distribution of target errors for the 3.5 m cable depth altimeter experiments of Section 5.1. As shown in the figure, the 8.0 m cable is less precise than the 3.5 m cable, with 95% of readings within ± 14 cm ($\sigma =7.0$ cm), still close to the desired ≈ 0.25 m resolution. The dispersion of target errors for the 8.0 m cable still improves on the ultrasonic and air-pressure altimeter modes, even when those modes use the shorter 3.5 m cable.

Figure 24 shows the step response between target depths at 0.5 m increments. Like the system with the 3.5 m cable under depth altimeter control, the configuration with an 8.0 m cable can transition precisely between target depths.

Because the 8.0 m cable allows the sensor payload to remain within ± 14 cm for nearly all readings, this means an 8.0 m cable might be viable for monitoring water properties down to a depth of 7.0 m, and we intend to explore this in future work.

6 Discussion

Overall Performance. The precision for the depth altimeter flight mode exceeds our expectations, especially while flying in wind gusts at 80% of the manufacturer's limit of $10.0\,\mathrm{m\,s^{-1}}$. The field tests demonstrated the effectiveness of using a single depth altimeter as the sole input to a depth controller, since the sensor is small, light, reasonably

affordable (30 USD), and fast (<20 ms). We believe that depth control of a sensory payload will enable dramatically better spatiotemporal resolution in shallow water science datasets with the advantages of quick deployment and redeployment by UAV without additional sensors.

For the 8.0 m cable, we attribute the increase in deviation in target depth compared to the 3.5 m cable (see Figure 23) to wind-induced oscillations in the portion of the cable exposed to air ($\approx$4 m of cable) due to 3.5 m s^{-1} winds. Further exploration is reserved for future work.

Depth Control in the Field vs. Simulation. Figure 25 shows a comparison between field and simulated target depth errors. The field data are depth readings in depth altimeter mode, and the simulated data is also depth altimeter mode and based on the 'All Disturbances Combined' simulation shown in Figure 10. As shown in the figure, the simulated results predict a tighter distribution of target errors ($\sigma =$1.9 cm) than what was encountered in the field ($\sigma =$4.2 cm). The simulation likely underestimates the impact of the interactions of parameters that cause the wider range of depth errors and the longer 'tails' in the distribution. Overall, the simulated precision is close to the precision observed in the field, and allowed us to explore relevant parameters quickly in simulation.

Lessons Learned In this work we have successfully developed a method to keep a UAV's cable-suspended payload at a precise depth in water. During development we experienced numerous instructive failures.

During development, we supposed that fusing data from multiple sensors might improve depth precision, but after characterizing and using the depth altimeter alone we do not see the benefit of additional sensors. This is primarily because other sensors measure the UAV's altitude, not the depth of the sensor payload. It could be useful to have two separate estimators, one for the air altitude and another for the depth. This is particularly useful when transitioning between having the sensor in and out of the water.

We started to build a such a controller that automatically switched between 'out-of-water' and the three 'in-water' modes, but found the switching controller to be too complicated, because it is challenging to foresee all the conditions that are required for a smooth switch. Instead, we found that for these experiments it was sufficient to have a human pilot manually fly the UAV into position over water, then switch to one of the three computer-controlled modes.

Flying over water with UAVs is challenges, because they are not water-hardened, and waterproofing can increase the system weight, reducing flight times. We considered adding flotation but have found that it interferes with the flight dynamics. We also considered (early on) landing on the water, but our water science partners were concerned about how this would mix the water.

Battery life is still a major factor. Speeding up sensor response times or having multiple sensors in a single payload could help this to scale.

7 Future Work

One future challenge includes integrating sensor payloads requested by water scientists. The challenge is that the irregular shapes and configurations of sensors might result in different drag and terminal velocities. We plan to apply depth control to a larger UAV (5 kg) because of payload and longer flight time, and potentially longer cables. We also would also like to explore UAV-based subsurface sensing with adaptive sampling. We examined the depth error as a function of lateral disturbance (error in x and y position), like when wind or GPS drift pushes the UAV out of position. However, we saw no relationship between lateral error and depth error. We plan to explore this in flowing water or while the UAV is translating in x and y.

A hybrid controller could switch between flight modes based on violations of invariants inferred during successful flights (Jiang et al., 2017) (like hitting the bed below the water, becoming entangled, or getting encased in muck). This approach requires positive examples and can be conservative, but is an automated way of detecting system anomalies.

Embedding the control on the UAV is a natural next step, using the radio link primarily for higher-level planning and safety controls. This could also be coupled with adaptive sampling or in coordinating with a team of vehicles.

There is interest is getting underwater video for other applications, but this might require a different cable like an optical data transfer cable. The primary challenge will be balancing the additional payload requirement both underwater and on the UAV platform.

In our previous work (Chung et al., 2015), we explored changing the cable length using an electric spooling mecha-

nism. We spooled the cable up during flight to avoid pendulum motions and then unspooled it while hovering over water to measure temperature. It might be possible to use the depth sensor to actively control the depth with the spool. This again is a trade-off of system complexity and payload.

Flying over water with micro UAVs that are not waterproof is inherently risky, and there are a number of ways to increase the reliability of this kind of system: 1) better protection from unsafe descent, including conductivity sensors on the cable near the UAV, and at least one ultrasonic sensor for redundant backup; 2) break-away cable with a buoy; 3) a protective cover for the depth altimeter to prevent fouling; and, 4) buoyancy of the UAV.

8 Conclusions

This work explores a novel method for precisely maintaining the target of a submerged sensor payload passively cabled to a UAV. Our method enables 95% of sensor payload readings within ± 8.2 cm of the target depth, increasing the depth resolution of UAV-based water property datasets. We conducted field experiments that validate the approach, resulting in a 75% reduction in standard deviation of depth readings ($\sigma = 4.2$ cm) compared with ultrasonic mode ($\sigma = 16.1$ cm), and air altimeter mode ($\sigma = 30.1$ cm) all with statistical significance. We tested our method in winds of $4-8$ m s^{-1} and the system still quickly and accurately reached and maintained target depths. The non-linear dynamics of a system with a semi-rigid cable are challenging to model as it interacts with wind and water. Still, we used simulation to guide and refine our approach before implementation. We also presented initial results for a longer, 8.0 m cable, the longest cabled sensor system yet attempted in UAV-based sub-surface water monitoring, and demonstrated that even at this length the approach allows water monitoring at precise depths ($\sigma = 7.0$ cm) from the air.

References

Achtelik, M. C., Doth, K.-M., Gurdan, D., and Stumpf, J. (2012). Design of a multi-rotor MAV with regard to efficiency, dynamics and redundancy. In *AIAA Guidance, Navigation, and Control Conference*, pages 1–17.

Akamatsu, Y., Watanabe, Y., Goto, M., Inui, R., Katano, I., Nagano, M., Takahara, T., Minamoto, T., et al. (2017). Water sampling for environmental DNA surveys by using an unmanned aerial vehicle. *Limnology and Oceanography: Methods*, 15(11):939–944.

Alam, T., Reis, G. M., Bobadilla, L., and Smith, R. N. (2018). A data-driven deployment approach for persistent monitoring in aquatic environments. In *Second IEEE International Conference on Robotic Computing, IRC 2018, Laguna Hills, CA, USA, January 31 - February 2, 2018*, pages 147–154. IEEE Computer Society.

Anderson, C. R., Sapiano, M. R., Prasad, M. B. K., Long, W., Tango, P. J., Brown, C. W., and Murtugudde, R. (2010). Predicting potentially toxigenic pseudo-nitzschia blooms in the chesapeake bay. *Journal of Marine Systems*, 83(3):127 – 140. GEOHAB Modeling.

Ascending Technologies (2012). AscTec Firefly Safety Sheet. `www.asctec.de/downloads/public/FF_AscTec-Firefly_safety-data-sheet.pdf`. Accessed: 2017-12-20.

Bershadsky, D., Haviland, S., Valdez, P. E., and Johnson, E. (2016). Design considerations of submersible unmanned flying vehicle for communications and underwater sampling. In *OCEANS 2016 MTS/IEEE Monterey*, pages 1–8.

Box, G. E. (1953). Non-normality and tests on variances. *Biometrika*, 40(4):318–335.

Brown, R. G. and Hwang, P. Y. (1997). Introduction to random signals and applied Kalman filtering: with MATLAB exercises and solutions. *Introduction to random signals and applied Kalman filtering: with MATLAB exercises and solutions, by Brown, Robert Grover.; Hwang, Patrick YC New York: Wiley, c1997.*

Burri, M., Oleynikova, H., Achtelik, M. W., and Siegwart, R. (2015). Real-time visual-inertial mapping, re-localization

and planning onboard MAVs in unknown environments. In *2015 IEEE/RSJ International Conference on Intelligent Robots and Systems (IROS)*, pages 1872–1878.

Chung, M., Detweiler, C., Hamilton, M., Higgins, J., Ore, J. P., and Thompson, S. (2015). Obtaining the thermal structure of lakes from the air. *Water*, 7(11):6467–6482.

Chung, M., Detweiler, C., Higgins, J., Ore, J., Dralle, D., and Thompson, S. (2016). Unmanned aerial system aids dry-season stream temperature sensing. In *AGU Fall Meeting Abstracts*.

Cruz, N. A. and Matos, A. C. (2008). The MARES AUV, a modular autonomous robot for environment sampling. In *OCEANS 2008*, pages 1–6.

Das, J., Py, F., Harvey, J. B., Ryan, J. P., Gellene, A., Graham, R., Caron, D. A., Rajan, K., and Sukhatme, G. S. (2015). Data-driven robotic sampling for marine ecosystem monitoring. *The International Journal of Robotics Research*, 34(12):1435–1452.

DeMario, A., Lopez, P., Plewka, E., Wix, R., Xia, H., Zamora, E., Gessler, D., and Yalin, A. P. (2017). Water plume temperature measurements by an unmanned aerial system (UAS). *Sensors*, 17(2):306.

Dodds, W. K. (2002). *Freshwater ecology: concepts and environmental applications*. Academic press.

Dodds, W. K., Bouska, W. W., Eitzmann, J. L., Pilger, T. J., Pitts, K. L., Riley, A. J., Schloesser, J. T., and Thornbrugh, D. J. (2009). Eutrophication of U.S. freshwaters: Analysis of potential economic damages. *Environmental Science & Technology*, 43(1):12–19.

Dunbabin, M. (2016). Autonomous greenhouse gas sampling using multiple robotic boats. In *Field and Service Robotics*, pages 17–30. Springer.

Eubank, R., Atkins, E., and Macy, D. (2009). Autonomous guidance and control of the Flying Fish ocean surveillance platform. In *AIAA Infotech@ Aerospace Conference*, pages 2009–2021.

Fischer, H. B., List, J. E., Koh, C. R., Imberger, J., and Brooks, N. H. (2013). *Mixing in inland and coastal waters*. Elsevier.

Fligner, M. A. and Killeen, T. J. (1976). Distribution-free two-sample tests for scale. *Journal of the American Statistical Association*, 71(353):210–213.

Garneau, M.-È., Posch, T., Hitz, G., Pomerleau, F., Pradalier, C., Siegwart, R., and Pernthaler, J. (2013). Short-term displacement of planktothrix rubescens (cyanobacteria) in a pre-alpine lake observed using an autonomous sampling platform. *Limnology and Oceanography*, 58(5):1892–1906.

Goodarzi, F., Lee, D., Lee, T., et al. (2014). Geometric stabilization of a quadrotor UAV with a payload connected by flexible cable. In *American Control Conference (ACC), 2014*, pages 4925–4930.

Higgins, J. and Detweiler, C. (2016). The Waterbug sub-surface sampler: Design, control and analysis. In *2016 IEEE/RSJ International Conference on Intelligent Robots and Systems (IROS)*, pages 330–337.

Hollinger, G. A. and Sukhatme, G. S. (2014). Sampling-based robotic information gathering algorithms. *The International Journal of Robotics Research*, 33(9):1271–1287.

Jain, S., Nuske, S., Chambers, A., Yoder, L., Cover, H., Chamberlain, L., Scherer, S., and Singh, S. (2015). Autonomous river exploration. In *Field and Service Robotics*, pages 93–106. Springer.

Jiang, H., Elbaum, S., and Detweiler, C. (2017). Inferring and monitoring invariants in robotic systems. *Autonomous Robots*, 41(4):1027–1046.

Kármán, T. V. (1937). The fundamentals of the statistical theory of turbulence. *Journal of the Aeronautical Sciences*, 4(4):131–138.

Koparan, C. and Koc, A. B. (2016). Unmanned aerial vehicle (UAV) assisted water sampling. In *2016 ASABE Annual International Meeting*, page 1. American Society of Agricultural and Biological Engineers.

Kudela, R. M., Anderson, C., Birch, J. M., Bowers, H., Caron, D. A., Chao, Y., Doucette, G., Farrara, J. D., Gellene, A. G., Negrey, K., Howard, M. D., Ryan, J. P., Scholin, C. A., Smith, J., and Sukhatme, G. (2015). Harmful Algal Bloom Hotspots Really Are Hot: A Case Study from Monterey Bay, California. *AGU Fall Meeting Abstracts*, pages OS51C–02.

Lawrance, N. R. J., Chung, J. J., and Hollinger, G. A. (2017). Fast marching adaptive sampling. *IEEE Robotics and Automation Letters*, 2(2):696–703.

Ma, K.-C., Liu, L., Heidarsson, H. K., and Sukhatme, G. S. (2017). Data-driven learning and planning for environmental sampling. *Journal of Field Robotics*.

MacIntyre, S., Romero, J. R., and Kling, G. W. (2002). Spatial-temporal variability in surface layer deepening and lateral advection in an embayment of lake victoria, east africa. *Limnology and oceanography*, 47(3):656–671.

Maxbotix (2018). MaxBotix Ultrasonic Sensors. `https://www.maxbotix.com/Ultrasonic_Sensors/MB1240.htm`. [Online; accessed 2-May-2018].

Measurement Specialties (2015). Pressure Sensor MS5803-01BA. `http://www.te.com/usa-en/product-CAT-BLPS0038.html`. Accessed: 2017-3-21.

Meyer, J., Sendobry, A., Kohlbrecher, S., Klingauf, U., and Von Stryk, O. (2012). Comprehensive simulation of quadrotor UAVS using ROS and Gazebo. In *International Conference on Simulation, Modeling, and Programming for Autonomous Robots*, pages 400–411. Springer.

Nuske, S., Choudhury, S., Jain, S., Chambers, A., Yoder, L., Scherer, S., Chamberlain, L., Cover, H., and Singh, S. (2015). Autonomous exploration and motion planning for an unmanned aerial vehicle navigating rivers. *J. Field Robotics*, 32(8):1141–1162.

Ore, J.-P. and Detweiler, C. (2018). Sensing water properties at precise depths from the air. In *Field and Service Robotics*, pages 205–220. Springer.

Ore, J. P., Elbaum, S., Burgin, A., and Detweiler, C. (2015). Autonomous aerial water sampling. *Journal of Field Robotics*, 32(8):1095–1113.

Ore, J. P., Elbaum, S., Burgin, A., Zhao, B., and Detweiler, C. (2013). Autonomous aerial water sampling. In *Proc. of The 9th Intl. Conf. on Field and Service Robots (FSR). Brisbane, Australia*, volume 5, pages 137–151.

Ribeiro, M., Ferreira, A. S., Gonçalves, P., Galante, J., and de Sousa, J. B. (2016). Quadcopter platforms for water sampling and sensor deployment. In *OCEANS 2016 MTS/IEEE Monterey*, pages 1–5.

Rodrigues, P., Marques, F., Pinto, E., Pombeiro, R., Lourenço, A., Mendonça, R., Santana, P., and Barata, J. (2015). An open-source watertight unmanned aerial vehicle for water quality monitoring. In *OCEANS'15 MTS/IEEE Washington*, pages 1–6.

Sanseverino, I., Conduto, D., Pozzoli, P., Dobricic, S., and Lettieri, T. (2016). Algal bloom and its economic impact. *EUR 27905 EN; doi: 10.2788*, 660478.

Schwarzbach, M., Laiacker, M., Mulero-Pazmany, M., and Kondak, K. (2014). Remote water sampling using flying robots. In *2014 International Conference on Unmanned Aircraft Systems (ICUAS)*, pages 72–76.

Shapiro, S. S. and Wilk, M. B. (1965). An analysis of variance test for normality (complete samples). *Biometrika*, 52(3/4):591–611.

Song, K., Brewer, A., Ahmadian, S., Shankar, A., Detweiler, C., and Burgin, A. J. (2017). Using unmanned aerial vehicles to sample aquatic ecosystems: Unmanned aerial vehicles in limnology. *Limnology and Oceanography: Methods*.

Tang, S. and Kumar, V. (2015). Mixed integer quadratic program trajectory generation for a quadrotor with a cable-suspended payload. In *2015 IEEE International Conference on Robotics and Automation (ICRA)*, pages 2216–2222.

United States Department of Defense (1997). *Flying Qualities Of Piloted Airplanes*. U.S. Military, MIL-HDBK-1797-F-8785C.

Yoo, S., Stuntz, A., Zhang, Y., Rothschild, R., Hollinger, G. A., and Smith, R. N. (2015). Experimental analysis of receding horizon planning algorithms for marine monitoring. In Wettergreen, D. and Barfoot, T. D., editors, *Field and Service Robotics - Results of the 10th International Conference, Toronto, Canada, 23-26 June 2015*, volume 113 of *Springer Tracts in Advanced Robotics*, pages 31–44. Springer.

Zhang, F., En-Nasr, O., Litchman, E., and Tan, X. (2015). Autonomous sampling of water columns using gliding robotic fish: Control algorithms and field experiments. In *2015 IEEE International Conference on Robotics and Automation (ICRA)*, pages 517–522.

|	SIMULATION PROPERTY	SYMBOL	VALUE
UAV	Mass including battery	m_u	$1.0\,\text{kg}$
	Air drag constant	$k_u = \frac{1}{2}\rho_a A_u C_u$	$0.010\,\text{kg}\,\text{m}^{-1}$
	Air density at $15\,^\circ\text{C}$	ρ_a	$1.23\,\text{kg}\,\text{m}^{-3}$
	Cross-sectional area	A_u	-
	Drag coefficient	C_u	-
	Wind force on UAV at $5.0\,\text{m}\,\text{s}^{-1}$	F_{wind}	$0.258\,\text{N}$
	Total thrust	F_{thrust}	*varies*
	Thrust opposing gravity	F_z	*varies*
CABLE	Link mass	m_l	$3.8\,\text{g}$
	Number of links	N_l	16
	Cable-payload mass	m_{CP}	$78.8\,\text{g}$
	Link length	L_l	$0.25\,\text{m}$
SUBMERGED PAYLOAD	Mass (Sensor & Housing)	m_p	$18\,\text{g}$
	Water drag constant	$k_p = \frac{1}{2}\rho_w A_p C_p$	$0.605\,\text{kg}\,\text{m}^{-1}$
	Water density at $15\,^\circ\text{C}$	ρ_w	$997\,\text{kg}\,\text{m}^{-3}$
	Cross-sectional area	A_p	-
	Drag coefficient	C_p	-
	Water drag force at $1\,\text{m}\,\text{s}^{-1}$	F_{drag}	$0.605\,\text{N}$
	Terminal velocity in water	v_t	$-0.54\,\text{m}\,\text{s}^{-1}$
	Depth altimeter sampling rate	d_r	$50\,\text{Hz}$
	Depth altimeter sensor delay	d_s	$100\,\text{ms}$
ENVIRONMENT	Air temperature	t_a	$15\,^\circ\text{C}$
	Air pressure	p_a	$101.325\,\text{kPa}$
	Water temperature	t_w	$15\,^\circ\text{C}$
	Gravity	g	$9.81\,\text{m}\,\text{s}^{-2}$
	Simulation Duration	t	$30\,\text{s}$
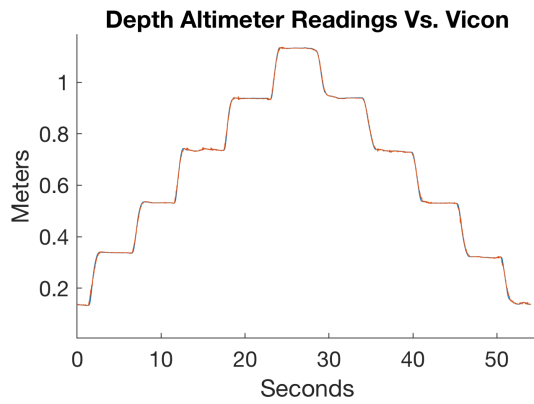
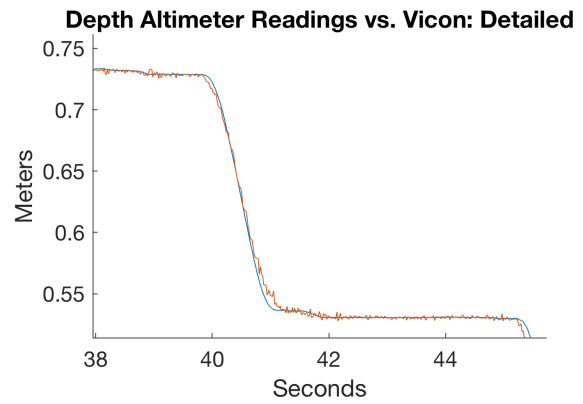**Figure 15:** Comparison of depth altimeter vs. Vicon.

Figure 16: Zoomed in comparison of depth altimeter readings to Vicon.
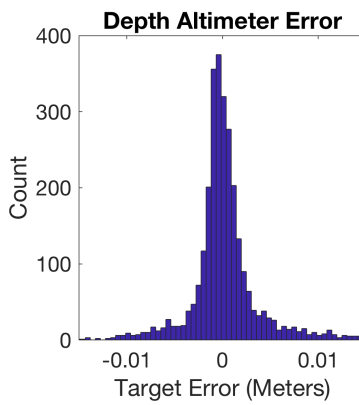

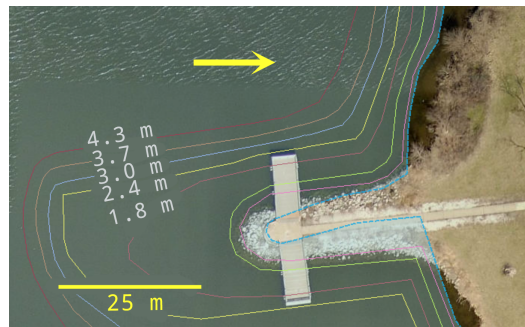**Figure 17:** Distribution of depth altimeter errors.

Figure 18: Wildwood Lake near Lincoln, Nebraska, USA, shown with depth contours. The yellow arrow indicates location of field experiments. Bathymetric map courtesy of Nebraska Game & Parks.
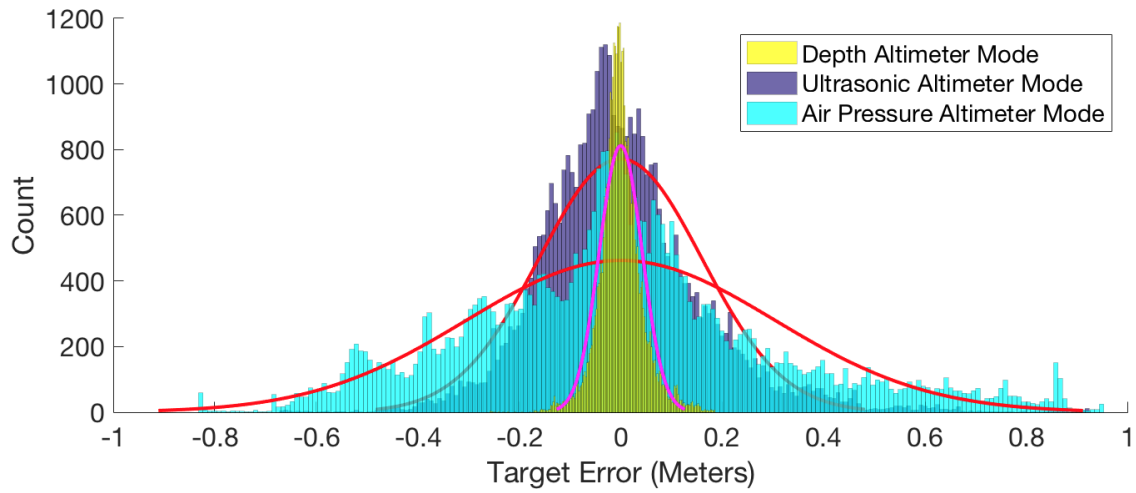
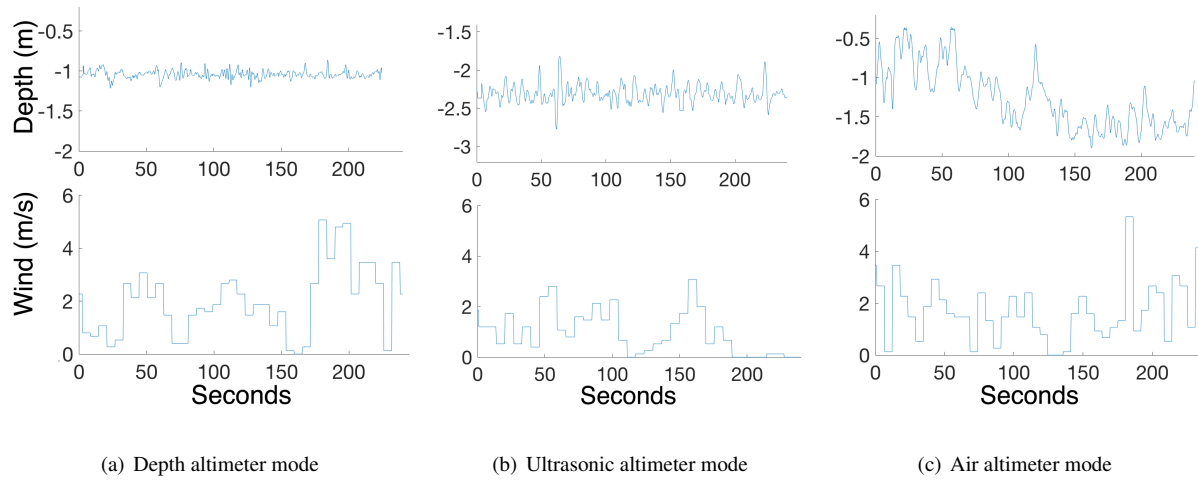**Figure 19:** Distribution of target depth error during three flight modes.

(a) Depth altimeter mode   (b) Ultrasonic altimeter mode   (c) Air altimeter mode

Figure 20: Examples of depth precision in the three different flight modes, showing 5-second-average wind speeds. Note that the *y*-axes of all depth figures span 1.8 m.
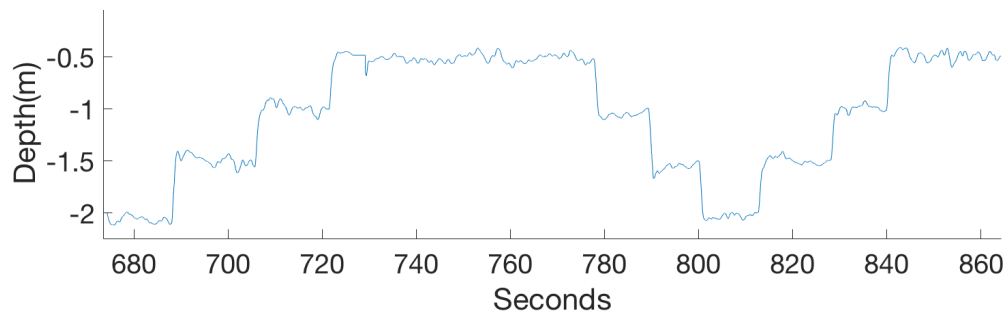
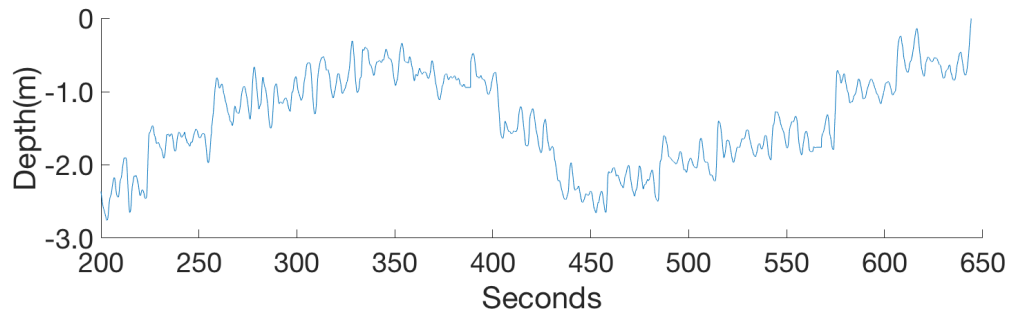**Figure 21:** Step response of depth altimeter mode at 0.5 m increments for a 3.5 m cable.

Figure 22: Step response of air pressure altimeter mode at 0.5 m increments for a 3.5 m cable.
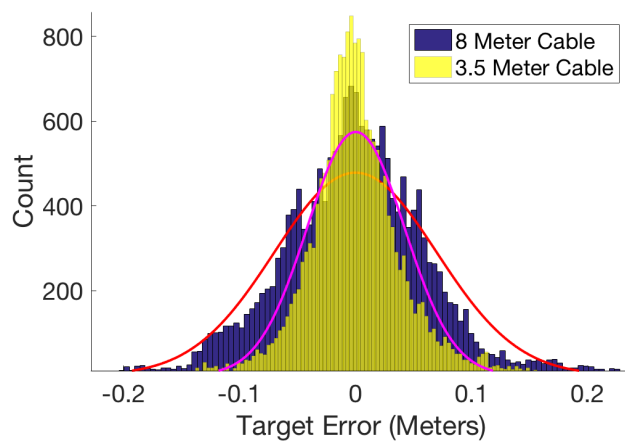

Figure 23: Target depth error comparison between 8.0 m and 3.5 m cables both using depth altimeter mode over 4 minutes of flight.
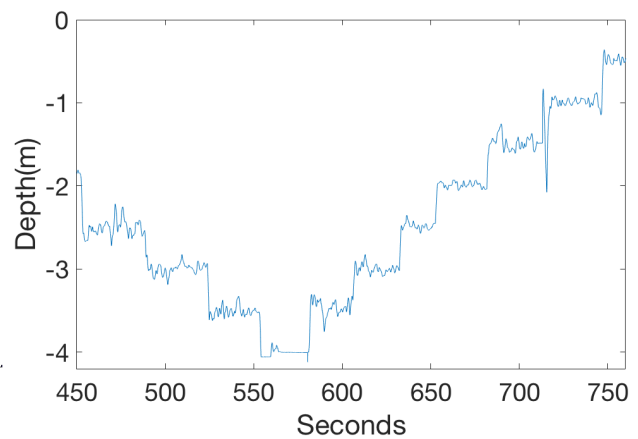

Figure 24: Step response to target depths at 0.5 m increments for an 8.0 m cable. Note the flat readings near 550 seconds indicating the water bottom.
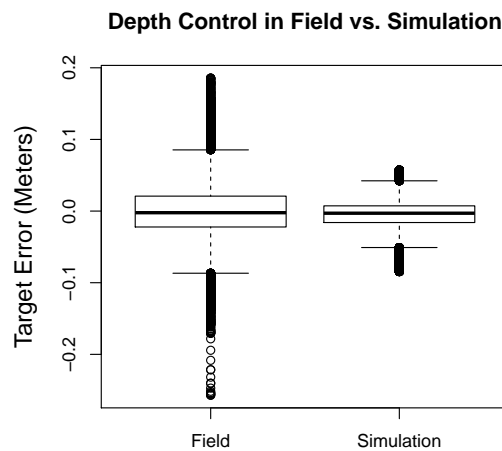

Figure 25: Comparison of depth control error between simulation and field experiments.